PNAS RESEARCH ARTICLE | PHYSICS

Observation of Weyl exceptional rings in thermal diffusion

Guoqiang Xu[a,1], Wei Li[b,1], Xue Zhou[c,1], Huagen Li[a,1], Ying Li[d,e], Shanhui Fan[f,g], Shuang Zhang[h,i], Demetrios N. Christodoulides[j], and Cheng-Wei Qiu[a,2]

Edited by Peter Rossky, Rice University, Houston, TX; received May 29, 2021; accepted February 3, 2022

A non-Hermitian Weyl equation indispensably requires a three-dimensional (3D) real/synthetic space, and it is thereby perceived that a Weyl exceptional ring (WER) will not be present in thermal diffusion given its purely dissipative nature. Here, we report a recipe for establishing a 3D parameter space to imitate thermal spinor field. Two orthogonal pairs of spatiotemporally modulated advections are employed to serve as two synthetic parameter dimensions, in addition to the inherent dimension corresponding to heat exchanges. We first predict the existence of WER in our hybrid conduction–advection system and experimentally observe the WER thermal signatures verifying our theoretical prediction. When coupling two WERs of opposite topological charges, the system further exhibits surface-like and bulk topological states, manifested as stationary and continuously changing thermal processes, respectively, with good robustness. Our findings reveal the long-ignored topological nature in thermal diffusion and may empower distinct paradigms for general diffusion and dissipation controls.

Weyl exceptional ring | spinor field | non-Hermitian topology | thermal diffusion

Significance

Thermal diffusion is dissipative and strongly related to non-Hermitian physics. At the same time, non-Hermitian Weyl systems have spurred tremendous interest across photonics and acoustics. This correlation has been long ignored and hence shed little light upon the question of whether the Weyl exceptional ring (WER) in thermal diffusion could exist. Intuitively, thermal diffusion provides no real parameter dimensions, thus prohibiting a topological nature and WER. This work breaks this perception by imitating synthetic dimensions via two spatiotemporal advection pairs. The WER is achieved in thermal diffusive systems. Both surface-like and bulk states are demonstrated by coupling two WERs with opposite topological charges. These findings extend topological notions to diffusions and motivate investigation of non-Hermitian diffusive and dissipative control.

The observation of Weyl points in Hermitian systems has generated tremendous interest in condensed matter physics (1), photonics (2–5), and acoustics (6, 7). As the counterpart of a magnetic monopole in momentum space (8), a Weyl point possesses a quantized Chern number and serves as the source of topologically nontrivial band curvatures in three-dimensional (3D) momentum space. It leads to a wide variety of novel phenomena, including Weyl nodal rings (9), Fermi arc states (6, 10), and chiral anomalies (11). Unlike the ideal lossless systems, gain and loss (12) in natural systems could break hermiticity, and exhibit the exclusive property of exceptional points (EPs) in non-Hermitian systems. The EPs contribute to the degeneracies at the coalescence of two or more eigenvectors (13) and further induce exotic phenomena of unconventional reflection and transmission (14), single-mode lasers (15, 16), light steering (17), and reversed pump dependence of lasers (18).

The recent discoveries in non-Hermitian photonics (19–23) and cold atomic systems (24) indicate that, in the presence of gain and/or loss, a Weyl point could expand into a ring of EPs (25), that is, a Weyl exceptional ring (WER) described by a non-Hermitian Weyl Hamiltonian $H(k) = v_x k_x \sigma_x + v_y k_y \sigma_y + v_z k_z \sigma_z + i\boldsymbol{\tau}\cdot\boldsymbol{\sigma}$, where $\boldsymbol{\tau} = (\tau_x, \tau_y, \tau_z)$, and its elements $\tau_{x,y,z}$ are real numbers that parameterize the nonhermicity added to the system. $\boldsymbol{\sigma} = (\sigma_x, \sigma_y, \sigma_z)$, while $\sigma_{x,y,z}$ denote the Pauli matrices. Such a WER serves as the source of Berry flux and preserves the Chern number, suggesting unexplored properties and exotic non-Hermitian topological transitions. As a typical dissipative system, thermal diffusion naturally corresponds to the non-Hermitian component of a Hamiltonian, thus hinting at the possible existence of WER in thermal systems. However, from a mathematical point of view, the thermal diffusion could only provide the non-Hermitian term ($i\boldsymbol{\tau}\cdot\boldsymbol{\sigma}$) in the non-Hermitian Weyl Hamiltonian, without any real parameter dimensions ($v_x k_x \sigma_x \approx v_z k_z \sigma_z$). Although the recently demonstrated antiparity time symmetry heat transfer (26, 27) indicates a connection between non-Hermitian property and classical thermal diffusion, the inherent absence of a spinor field, requiring anticommutation associated with all three dimensions, fundamentally makes the WER elusive in thermal transport.

Results

One of the preferred experimental means of demonstrating the WER in photonics is to create helical waveguides (20) possessing helicoidal properties. As shown in Fig. 1*A*, each spinor field could effectively decouple into two periodic projections in two orthogonal spaces. Conversely, the effective spinor field could also be established via assembly of components in the corresponding orthogonal spaces with a $\pi/2$ relative

Author contributions: G.X., X.Z., and C.-W.Q. designed research; G.X., W.L., X.Z., H.L., and C.-W.Q. performed research; G.X., W.L., X.Z., H.L., Y.L., and C.-W.Q. contributed new reagents/analytic tools; G.X., W.L., X.Z., H.L., Y.L., S.F., S.Z., D.N.C., and C.-W.Q. analyzed data; and G.X., W.L., H.L., S.F., S.Z., D.N.C., and C.-W.Q. wrote the paper.

The authors declare no competing interest.

This article is a PNAS Direct Submission.

[1]G.X., W.L., X.Z., and H.L. contributed equally to this work.

[2]To whom correspondence may be addressed. Email: chengwei.qiu@nus.edu.sg.

This article contains supporting information online at http://www.pnas.org/lookup/suppl/doi:10.1073/pnas.2110018119/-/DCSupplemental.

Published April 4, 2022.

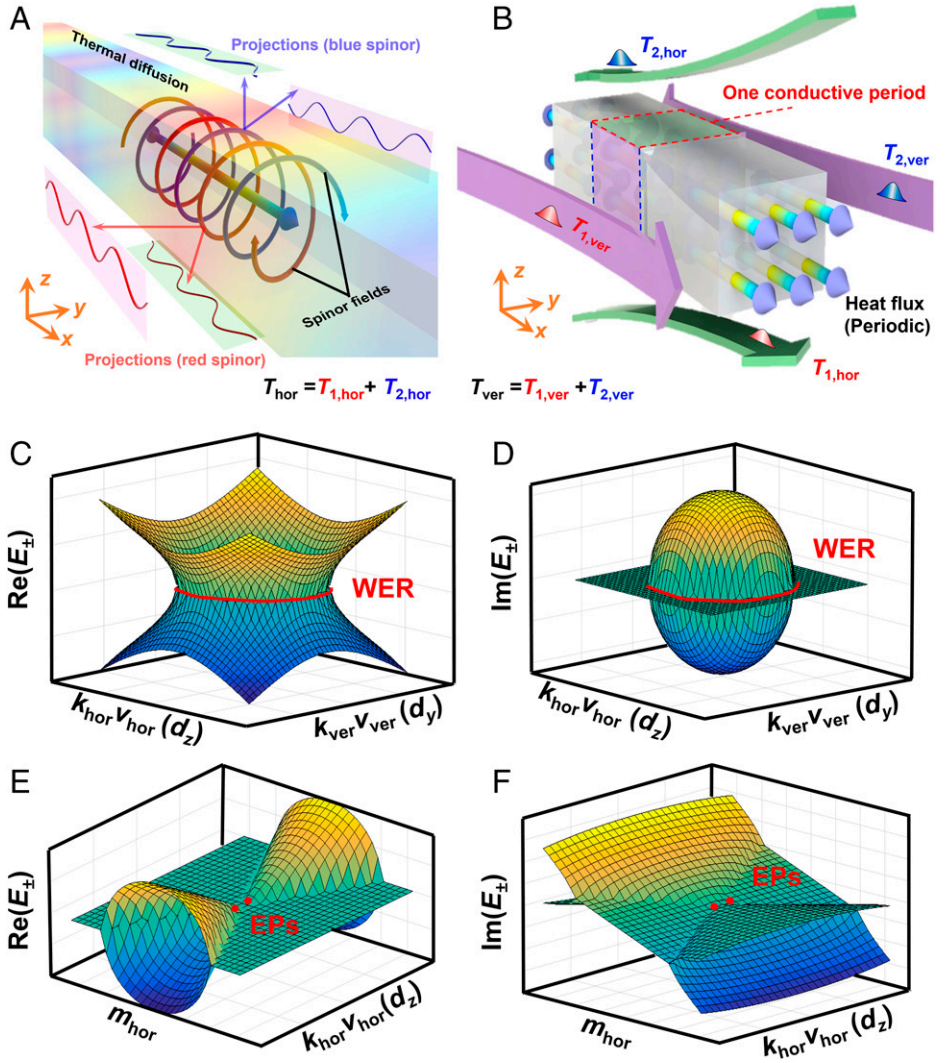

Fig. 1. Non-Hermitian diffusive system and corresponding band structure supporting a WER. (*A*) Schematic of the helicities in periodic thermal diffusion around the existing heat flux. The light green and light purple regions respectively denote the orthogonal surfaces holding the projections of the red and blue advective spinor fields, while the red and blue curves on these surfaces denote the orthogonal projections of corresponding spinor fields. (*B*) An underlying model supporting a WER in non-Hermitian diffusive system coupled with four counter advections in orthogonal surfaces. The periodic heat flux colored in rainbow inside the central medium indicates the initial thermal distributions. (*C* and *D*) The band structures in the d_y–d_z plane under the condition of $m_{ver} = 0$ possessing a WER (marked in red). (*E* and *F*) The band structures in the $i{\cdot}m_{hor}$–d_z plane exhibiting two EPs for $k_{ver}v_{ver} = 0$, (m_{ver} is also vanished due to the lack of orthogonal advection). The correspondents of these two EPs can be found in the WER shown in *C* and *D*, while the $i{\cdot}m_{hor}$–d_z plane also intersects the d_y–d_z plane twice through the pair of EPs.

phase retardation. Thus, the effective helicities can be subsequently realized with these spinor fields. We consider a system consisting of a static medium strip of finite length surrounded by four spatiotemporally modulated counter advections along the periodic heat flux in orthogonal spaces (Fig. 1*B*). Here, the advections on the upper and bottom surfaces (green arrows) are regarded as the horizontal advections, while the others (purple arrows) on the lateral sides are defined as the vertical advections. Although the advections illustrated in Fig. 1*B* are imposed on orthogonal spaces, their propagative directions are all along the $\pm x$ axis, that is, the direction of periodic heat flux. That is, the periodic heat flux is simultaneously affected by the four advective projections of spinor fields in the orthogonal x–y and x–z spaces. Therefore, we can further divide the systematic thermal process into two subparts: 1) the heat transfer in the x–y space (affected by green arrows) and 2) the heat transfer in the x–z space (affected by purple arrows). The coupled thermal system, considering the hybrid thermal effects, leads to the following thermal processes:

Thermal process in the x–y space:

$$\rho c\frac{\partial T_{\rm hor}}{\partial t} = \underbrace{\left[\kappa\frac{\partial^2 T_{1,\rm hor}}{\partial x^2} + \rho c v_{1,\rm hor}\frac{\partial T_{1,\rm hor}}{\partial x} + \frac{h_{1,\rm hor}}{b_{1,\rm hor}}(T_{2,\rm hor} - T_{1,\rm hor})\right]}_{\text{Parallel thermal process in } +x \text{ direction}} + \underbrace{\left[\kappa\frac{\partial^2 T_{2,\rm hor}}{\partial x^2} + \rho c v_{2,\rm hor}\frac{\partial T_{2,\rm hor}}{\partial x} + \frac{h_{2,\rm hor}}{b_{2,\rm hor}}(T_{1,\rm hor} - T_{2,\rm hor})\right]}_{\text{Parallel thermal process in } -x \text{ direction}},$$

Thermal process in the x–z space:

$$\rho c\frac{\partial T_{\rm ver}}{\partial t} = \underbrace{\left[\kappa\frac{\partial^2 T_{1,\rm ver}}{\partial x^2} + \rho c v_{1,\rm ver}\frac{\partial T_{1,\rm ver}}{\partial x} + \frac{h_{1,\rm ver}}{b_{1,\rm ver}}(T_{2,\rm ver} - T_{1,\rm ver})\right]}_{\text{Orthogonal thermal process in } +x \text{ direction}} + \underbrace{\left[\kappa\frac{\partial^2 T_{2,\rm ver}}{\partial x^2} + \rho c v_{2,\rm ver}\frac{\partial T_{2,\rm ver}}{\partial x} + \frac{h_{2,\rm ver}}{b_{2,\rm ver}}(T_{1,\rm ver} - T_{2,\rm ver})\right]}_{\text{Orthogonal thermal process in } -x \text{ direction}}, \quad [1]$$

where $T_{\rm hor}$ and $T_{\rm ver}$ indicate the temperature fields of the two subparts respectively affected by the green and purple advective arrows shown in Fig. 1*B*, while ρ, c, and κ denote the density, specific heat, and thermal conductivity of the employed strip. As illustrated in Fig. 1*B*, each temperature field $T_{\rm hor}$ or $T_{\rm ver}$ can be effectively described with the thermal couplings affected by the corresponding horizontal advections in the x–y space or

vertical advections in the x–z space. Thus, we further employ $T_{1,\mathrm{hor}}$ ($T_{1,\mathrm{ver}}$) and $T_{2,\mathrm{hor}}$ ($T_{2,\mathrm{ver}}$) to indicate the partial temperature fields affected by corresponding advections (Fig. 1*B*). While $h_{1,\mathrm{hor}}$ ($h_{1,\mathrm{ver}}$) and $h_{2,\mathrm{hor}}$ ($h_{2,\mathrm{ver}}$) are the horizontal (vertical) advection heat transfer coefficients in x–y (x–z) space, $b_{1,\mathrm{hor}}$, $b_{2,\mathrm{hor}}$, $v_{1,\mathrm{hor}}$ and $v_{2,\mathrm{hor}}$ ($b_{1,\mathrm{ver}}$, $b_{2,\mathrm{ver}}$, $v_{1,\mathrm{ver}}$ and $v_{2,\mathrm{ver}}$) are the thicknesses and velocities of advective components imposing on the green (purple) surfaces in x–y (x–z) space. For simplification under small conductivity, we make $b_1 = b_2 = b$, and $v_1 = -v_2 = v$ in these advective components.

The effectively advective helicities are obtained along the periodic heat flux, owing to the two counter advection pairs respectively on the orthogonal x–y and x–z spaces. Such an orthogonal advective field would further contribute to the field couplings between the two subparts, thus leading to the nonuniform distributions relative to the initial heat flux inside the central strip under a small enough thermal conductivity κ. To describe such couplings, we employ the multiplication of "i" on the hybrid thermal process in the x–z space, in analog to the well-established description of orthogonal electric and magnetic fields in electromagnetics. Thus, the direction of the vertical thermal process in x–z space can be mathematically indicated, that is, $i\cdot\left(\kappa\frac{\partial^2 T_{1,\mathrm{ver}}}{\partial x^2}+\rho c v_{1,\mathrm{ver}}\frac{\partial T_{1,\mathrm{ver}}}{\partial x}+\frac{h_{1,\mathrm{ver}}}{b_{1,\mathrm{ver}}}\cdot\Delta T_{\mathrm{ver}}\right)+i\cdot\left(\kappa\frac{\partial^2 T_{2,\mathrm{ver}}}{\partial x^2}+\rho c v_{2,\mathrm{ver}}\frac{\partial T_{2,\mathrm{ver}}}{\partial x}+\frac{h_{2,\mathrm{ver}}}{b_{2,\mathrm{ver}}}\cdot\Delta T_{\mathrm{ver}}\right)$. Then, the judiciously counter advections lead to effective "oscillations" on the orthogonal surfaces of the two subparts, while the inherent conduction acts as the systemic dissipation. The partial thermal process in Eq. **1** can be rewritten with the following effective Hamiltonian H:

$$H=\begin{bmatrix}-i\left(D\cdot\left(k_{\mathrm{hor}}^2+ik_{\mathrm{ver}}^2\right)+m_{\mathrm{hor}}+im_{\mathrm{ver}}\right)+k_{\mathrm{hor}}v_{\mathrm{hor}} & i\left(m_{\mathrm{hor}}+im_{\mathrm{ver}}+k_{\mathrm{ver}}v_{\mathrm{ver}}\right)\\ i\left(m_{\mathrm{hor}}+im_{\mathrm{ver}}-k_{\mathrm{ver}}v_{\mathrm{ver}}\right) & -i\left(D\cdot\left(k_{\mathrm{hor}}^2+ik_{\mathrm{hor}}^2\right)+m_{\mathrm{hor}}+im_{\mathrm{ver}}\right)-k_{\mathrm{ver}}v_{\mathrm{ver}}\end{bmatrix}, \quad [2]$$

where $D=\kappa/\rho c$ is the diffusivity, while m_{hor} and m_{ver} respectively denote the endothermic or exothermic thermal exchanges in the x–y and x–z spaces that can be defined as $h_{\mathrm{hor}}/\rho c b_{\mathrm{hor}}$ and $h_{\mathrm{ver}}/\rho c b_{\mathrm{ver}}$; k_{hor} and k_{ver} are the effective wavenumbers of the horizontal and vertical components relative to the imposed advections. For generality, we make the central strip length L as the characteristic motion lengths along x direction in one period, that is, the effective wavelengths, for the oscillatory advections respectively in the x–y and x–z spaces. Thus, the effective wavenumbers can be expressed as $k_{\mathrm{hor}}=k_{\mathrm{ver}}=1/L$, and the first mode of the periodic temperature field can be observed on the central strip. It is worth noting that multiple modes with more than one periodic temperature field can be realized when we make the wavenumber $k_{\mathrm{hor}}=k_{\mathrm{ver}}=\mathrm{n}/L$ (n is an integer). Considering their consistent physics and experimental conveniences, we take the first mode as the representation in this work. Such an implementation effectively produces three synthetic dimensions (28–30), including two parameter dimensions of the spatiotemporally modulated horizontal ($k_{\mathrm{ver}}v_{\mathrm{ver}}$) and vertical ($k_{\mathrm{hor}}v_{\mathrm{hor}}$) advections for achieving the helicities, and one arising from the vertical heat exchange (m_{ver}) for matching the non-Hermitian Weyl Hamiltonian. Then, Eq. **2** can be written as $H=(i\cdot m_{\mathrm{hor}}-m_{\mathrm{ver}})\sigma_x-k_{\mathrm{ver}}v_{\mathrm{ver}}\sigma_y+k_{\mathrm{hor}}v_{\mathrm{hor}}\sigma_z-i\cdot(Dk_{\mathrm{hor}}{}^2+i\cdot Dk_{\mathrm{ver}}{}^2+m_{\mathrm{hor}}+i\cdot m_{\mathrm{ver}})I_{2\times 2}$, and the eigenvalues are

$$E_{\pm}=-i\left(\left(D\cdot\left(k_{\mathrm{hor}}^2+ik_{\mathrm{ver}}^2\right)+m_{\mathrm{hor}}+im_{\mathrm{ver}}\right)\pm\sqrt{\left(m_{\mathrm{hor}}\right)^2-\left(k_{\mathrm{hor}}v_{\mathrm{hor}}\right)^2-\left(k_{\mathrm{ver}}v_{\mathrm{ver}}\right)^2-\left(m_{\mathrm{ver}}\right)^2+2i\cdot m_{\mathrm{hor}}\cdot m_{\mathrm{ver}}}\right), \quad [3]$$

where the real space vectors can be indicated as $d_x=-m_{\mathrm{ver}}$, $d_y=-k_{\mathrm{ver}}v_{\mathrm{ver}}$, and $d_z=k_{\mathrm{hor}}v_{\mathrm{hor}}$. This eigenvalue would lead to a WER with a constant non-Hermitian horizontal heat exchange (m_{hor}) shown in Fig. 1 *C* and *D*. Besides, there exists a nearly flat real band within the WER (Fig. 1*C*), corresponding to the domains between the EP pair with small advective velocities in the complex plane of $i\cdot m_{\mathrm{hor}}-k_{\mathrm{hor}}v_{\mathrm{hor}}$ (d_z) as illustrated in Fig. 1 *E* and *F*.

The topological charge γ defined by the integral of Berry curvature across a closed surface can be used to describe the quantized invariant of such diffusion. It could possess different values when all or part of the WER is enclosed by the sphere integration surface (20) in the three synthetic dimensions (m_{ver}, $k_{\mathrm{ver}}v_{\mathrm{ver}}$, $k_{\mathrm{hor}}v_{\mathrm{hor}}$) (*SI Appendix*, Eq. S9). As illustrated in Fig. 2*A*, the topological charge γ of such a diffusion system can be ±1 if the synthetic surface of integration encloses the entire WER, and γ is zero if the whole integration surface is within or outside the WER (*SI Appendix*, *Supplementary Note 1*). Then, we study the non-Hermitian topological transitions based on the observed WER in diffusion under the three spatiotemporally modulated parameters of m_{ver}, $k_{\mathrm{ver}}v_{\mathrm{ver}}$, and $k_{\mathrm{hor}}v_{\mathrm{hor}}$. The representative scheme and setups are presented in Fig. 2*B*. The sample consists of three parts as illustrated in Fig. 2 *B*, *Lower Inset*, that is, the conductive component of the central white strip, the horizontal advection components including two green counter motional hollow strips on the upper and bottom surfaces, and the vertical advection components consisting of another two red counter motional solid strips on the lateral surfaces. Here, we elaborate the topological transitions via two typical cases with different spatiotemporally modulated velocities (*Materials and Methods*). Both the nontrivial and trivial behaviors can be indicated by tracking the trajectories of the maximum temperature locations T_{max} in the measured surfaces as illustrated in Fig. 2 *B*, *Upper Inset*.

The experimental temperature profiles and the locations T_{max} of the measured surfaces are illustrated in Fig. 2 *B*–*F*, while the experimental thermal profiles at specific moments are shown in Fig. 2 *B*, *Insets* and *SI Appendix*, Fig. S1. When the surface of integration encircles the whole WER in case 1, the temperature profiles almost remain stationary in all directions as shown in Fig. 2 *C* and *D*. Such stationary temperature profiles during the encircling process indicate a constant Berry phase (24) of $\pm\pi$, thus further verifying the quantized topological charges of ±1 and the corresponding nontrivial topological transitions in this 3D non-Hermitian diffusion system (*SI Appendix*, Eqs. S6–S8). It is worth noting that the integration surface is outside the WER in case 2, and only zero Berry phases and quantized zero topological charge can be observed in *SI Appendix*, Eqs. S6 and S8 revealing trivial behaviors.

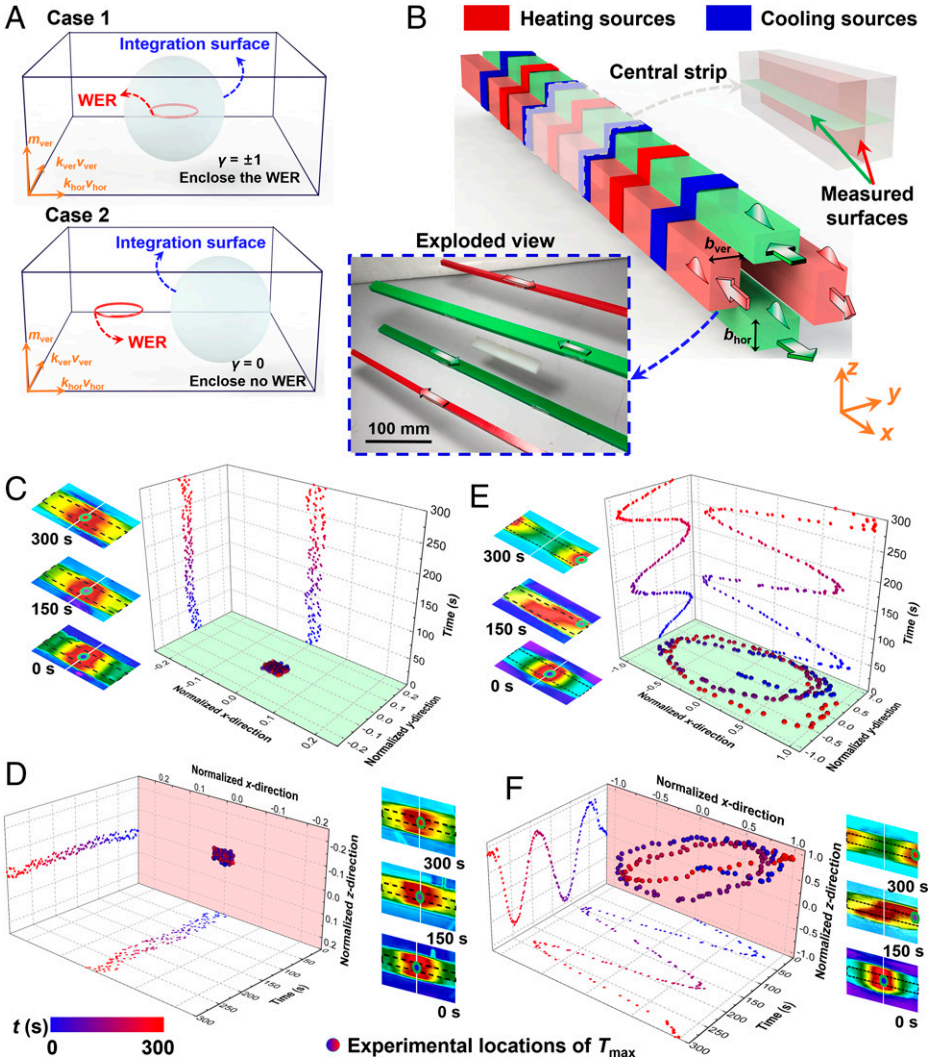

Fig. 2. Structure of the proposed cases and their phase transitions under time evolution advections. (*A*) The sphere evaluation surfaces of cases (*Upper*) 1 and (*Lower*) 2. (*B*) A representative scheme of observing topological behaviors around a WER. The heating and cooling sources are periodically and alternatively configured on the entire system for observing the initial thermal profile. (*Upper Inset*) The central strip and (*Lower Inset*) its decompositions. The horizontal and vertical temporal evaluation advections are imposed by the green and red strips through conveyor belts after the heating and cooling process, while the arrows indicate the initial motion directions of these strips. (*C* and *D*) The topologically nontrivial transitions of case 1 with unchanged profiles and (*E* and *F*) the trivial transitions of case 2 with continuously changing profiles. Among them, the normalized experimental phase trajectories of T_{max} on these measured surfaces are indicated by the colored balls according to the time, while their projections along specific directions are also presented on their lateral surfaces.

Thus, the continuously changing thermal profiles and T_{max} locations along all directions can be observed in case 2 as shown in Fig. 2 *E* and *F*, and the advective terms play the dominant roles in the thermal process. Note that we take the changing advective amplitudes as the synthetic dimensions to create the enclosing loop. Thus, the modulated frequencies of velocities have no effect on the size of the adopted enclosing loops (*SI Appendix*, *Supplementary Note 2*, *Supplementary Note 3*, *Supplementary Note 4*, and *Supplementary Note 5*).

One intriguing consequence relating to the WER is the surface-like state connecting the projections of two WERs with opposite topological charges in the synthetic surface of $m_{ver} - k_{ver}v_{ver}$ related to the vertical advections (Fig. 3*A*). Here, we theoretically calculate the effective spectra of a non-Hermitian thermal system coupled with opposite WERs along the changing vertical velocities ($k_{ver}v_{ver}$) and plot the real and imaginary parts of the spectra in Fig. 3 *A*, *Bottom*. As a representation, we make $|k_{hor}v_{hor}| = |k_{ver}v_{ver}|$ in this calculation. It is interesting that we can also theoretically observe the surface-like states in such a thermal system. These surface-like states connect the adjacent bands possessing opposite topological charges of ±1. To further confirm such unique surface-like state in thermal diffusion, we propose a coupled advective configuration in Fig. 3 *B* and *C* by positioning an additional conduction–advection setup side by side with the initial one in Fig. 2*B*. Such an implementation spontaneously provides a counter configuration of the vertical advection pair to the initial one and an opposite integral direction in *SI Appendix*, Eq. S8, thus further contributing to an opposite topological charge in the insert system (*Materials and Methods*). Then, we trace the experimental T_{max} locations and their projections onto the two measured surfaces (Fig. 3 *D*–*G*). These characteristic positions almost remain stationary with a robust thermal process between these central strips, as if they directly connect without surrounding advections. Such a robust heat transfer can be regarded as the distinct surface-like state in thermal diffusion, which exists on the synthetic plane of $m_{ver} - k_{ver}v_{ver}$ and connects the two WERs with opposite topological charges. Such a surface-like state can be indentified by the energy balance between the two coupling systems through the heat exchanges around the shared vertical advection, while the oscillated m_{ver} indicates the exothermic or endothermic exchanges of the two coupling subsystems. We further remove the pairs of WERs from the surface of integration. In this case, the analog of the bulk state

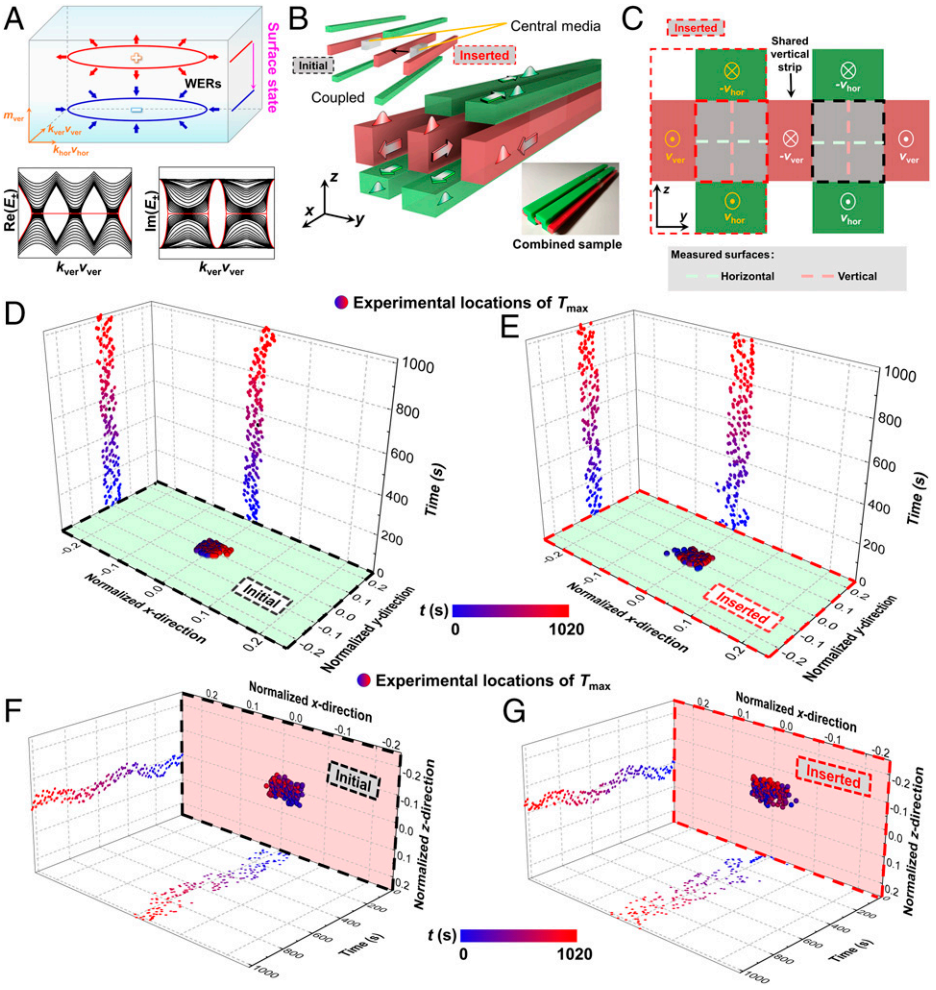

Fig. 3. Surface-like state and its topological transition in a thermal diffusion. (*A*) (*Top*) Surface-like state (pink line) connecting the projections of the opposite-charge WERs on the synthetic surface of m_{ver}-$k_{ver}v_{ver}$, while the red and blue arrows are the Berry fluxes. (*Bottom*) Illustrations of the real and imaginary parts of the effective spectra with respect to $k_{ver}v_{ver}$ for $|k_{hor}v_{hor}| = |k_{ver}v_{ver}|$ and $m_{hor} = 0.3\ s^{-1}$. The red lines indicate the surface-like state. (*B*) The modified structure with an inserted system. (*C*) The cross-sectional views of the advective configurations in the *y*–*z* space. The nontrivial transitions around the surface-like state on the (*D* and *E*) horizontal and (*F* and *G*) vertical measured surfaces as indicated in *C* (light green and light red). *D* and *F* denote the experimental trajectories of T_{max} of the initial system (black borders), while *E* and *G* present the experimental trajectories of T_{max} of the inserted system (red borders).

(*SI Appendix*, *Supplementary Note 8*) possessing zero topological charges with moving locations of T_{max} in the two central strips can be obtained as shown in Fig. 4. The temperature profiles of the surface-like and bulk states at specific moments are respectively presented in *SI Appendix*, Figs. S7 and S9. They indicate that both the initial and inserted central strips maintain the similarly stationary distributions in all directions for the surface-like state, revealing the robust heat transfer between the two strips. On the contrary, during the entire heat transfer process of the bulk state, the temperature profiles of the initial and inserted central strips keep moving, thus indicating the continuous phase changes in the thermal distributions and the absence of robustness in heat transfer between the two central strips. It is worth noting that all the nontrivial and trivial states shown in Figs. 2–4 are related to the robustness of the thermal profiles, that is, the relative locations of the temperature distributions. Due to the strong dissipative nature of thermal diffusion, their temperature magnitudes could relax to the average of the highest and lowest temperatures of the initial inputs without external sources, when the systems reach steady states.

Discussion

This work reveals that a hybrid conduction–advection thermal system with two sets of orthogonally spatiotemporally modulated advections could support a WER. These spatiotemporally modulated advections provide two artificial parameter dimensions and create the critical spinor fields in thermal diffusion. The concomitant heat exchanges further offer an additional synthetic dimension to match the non-Hermitian Weyl Hamiltonian. Observations of non-Hermitian thermal transitions around the WERs enable unexpected topological studies in macroscopic heat transfer. Such a platform holds the possibility of discovering more exotic behaviors in heat transfer, such as the chiral anomaly and nontrivial transitions. It might provide a distinct avenue for manipulating generally diffusive systems (31–34).

Materials and Methods

Fabricated Sample and General Setups for Observing the WER. The fabricated samples are illustrated in *SI Appendix*, Figs. S1*A* and S5*A*. The entire sample is held by four conveyor belts, which are fabricated by rubber with a conductivity of 0.4 $W{\cdot}m{\cdot}K^{-1}$. All the motional strips are made of polycaprolactam (PA6) with a thermal conductivity of 1.2 $W{\cdot}m^{-1}{\cdot}K^{-1}$, while the green strips are fabricated to a hollow structure to maintain 0.2 times the effective density of the red strips. For the central white strip, the horizontal and vertical thicknesses are, respectively, $d_{hor} = 5$ mm and $d_{ver} = 10$ mm, while the length L is 100 mm (Fig. 2*B*). To create the effective periodic thermal process, the advective strips should be much longer than the central one ($L_{hor} = L_{ver} > L$). Hence, we

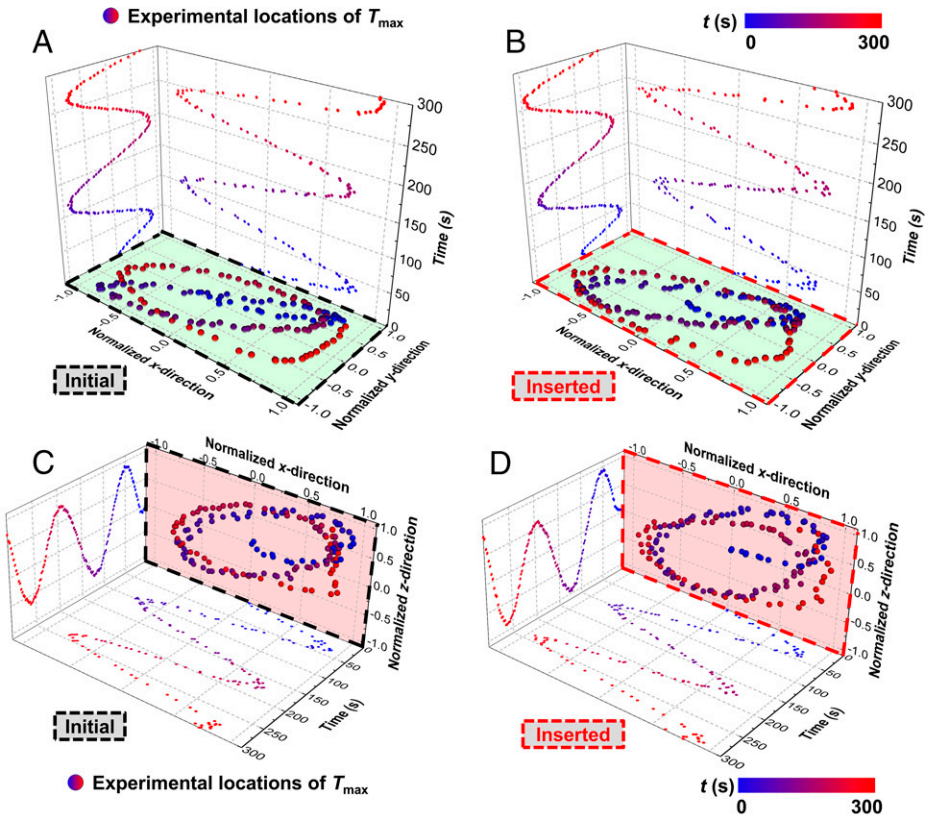

Fig. 4. Trivial transitions of the Bulk state under temporal evolution advections. The trivial transitions of the bulk states on the (*A* and *B*) horizontal and (*C* and *D*) vertical measured surfaces as indicated in Fig. 3*C* and *SI Appendix*, Fig. S7*A* (light green and light red). *A* and *B* illustrate the experimental phase trajectories of T_{max} of the initial system (black borders), while *C* and *D* are the experimental phase trajectories of T_{max} of the inserted system (red borders).

representatively make the structural parameters of the horizontal and vertical advection components $b_{hor} = b_{ver} = 5$ mm, and $L_{hor} = L_{ver} = 3L$ (*SI Appendix*, Fig. S5). The material properties are $\rho = 1{,}150$ kg·m^{-3}, $c = 1{,}400$ J·kg^{-1}·m^{-3}, and $\kappa = 1.2$ W·m^{-1}·K^{-1} for the central strip, and $\rho = 1{,}140$ kg·m^{-3}, $c = 1{,}640$ J·kg^{-1}·m^{-3}, and $\kappa = 1.2$ W·m^{-1}·K^{-1} for PA6 used in the red advective strips ($\rho_{eff} = 228$ kg·m^{-3}, $c_{eff} = 1{,}128$ J·kg^{-1}·m^{-3}, and $\kappa_{eff} = 0.26$ W·m^{-1}·K^{-1} for the green hollow advective strips). Each motional strip is connected to a conveyor belt, which is controlled by a correspondingly independent motor. The motors are driven by their actuators, and two motion controllers are employed to respectively manipulate the velocities of horizontal and vertical advections. Furthermore, grease with a conductivity of 1.2 W/m·K ($\rho = 1{,}150$ kg·m^{-3}, $c = 1{,}400$ J·kg^{-1}·m^{-3}) is also added in the interspace between the central and advective strips. The initial temperature field is imposed by periodically and alternatively configuring the heating and cooling strips on the combined sample of Figs. 2*B* and 3*B* as shown in *SI Appendix*, Fig. S5. The periodic distributions of multiple heating strips with a fixed temperature of 353 K provide the heating sources, while the interval of two adjacent heating strips is 100 mm. The other parts are cooled by cooling strips with a fixed temperature of 273 K. The entire heating processes for each case last for 30 min to observe the stably initial thermal profiles. All the thermal profiles are captured by a Flir infrared (IR) camera with the setting emissivity of 0.97, while the T_{max} locations are measured by fine-wire thermocouples embedded in the central strip. After achieving the steady and periodic thermal distributions, the motional strips are activated to study the transitions (*SI Appendix*, *Supplementary Note 6*).

Experimental Demonstrations for Surface-Like and Bulk States. Except for the previous system, another three motional strips and one central strip should be employed to construct the inserted system shown in Fig. 3 *B* and *C* and *SI Appendix*, Fig. S6, while seven belts are employed to support the initial and inserted advections. The strategy for realizing two opposite-charge WERs with the initial and inserted system can be found in *SI Appendix*, *Supplementary Note 7*. The same/opposite motional strategies of the horizontal/vertical advections of cases 1 and 2 are employed in the inserted systems. The parameters of the additional advective and central strips are same as the ones in the initial system, and grease with a conductivity of 1.2 W/m·K ($\rho = 1{,}150$ kg·m^{-3}, $c = 1{,}400$ J·kg^{-1}·m^{-3}) is also added within their intervals. The same heating strategy and boundary conditions are also employed. We first assemble the inserted system onto the previous one, and then heat the entire system (both the initial and inserted systems) for 30 min together. After the heating process, we implement motion functions in each strip via the motion controllers and motors. For the measurements, all the temperature profiles in the contents are measured by a Flir IR camera at specific moments. Since the changing trends of the surface and interface temperature profiles of the central strip are similar during the processes, we indirectly measure surface temperatures of the central strip using the IR camera to qualitatively indicate the transitions. For directly and accurately capturing T_{max} on the interfaces, we employ multiple fine-wire thermocouples which are embedded inside the central strip. For presenting the T_{max} locations at specific moments with respect to the initial locations at 0 s on these measured surfaces, we adopt normalized spatial dimensions to demonstrate the behaviors. Since the initial T_{max} locations (0 s) are at the centers of the horizontal and vertical surfaces, we take these centers as the origins and create local coordinates for normalizations on these two measured surfaces. Then, the normalized spatial dimensions can be obtained via dividing the collected positions (centered on the initial T_{max} locations) by half of the length/width/height of the measured surfaces, that is, $x^* = \frac{x}{L/2}$, $y^* = \frac{y}{d_{ver}/2}$, and $z^* = \frac{z}{d_{hor}/2}$, where L, d_{ver}, and d_{hor} are the length, width, and height of the central strip. *SI Appendix*, Fig. S8 *C* and *D* provides the graphical illustrations of the normalizations on each surface.

Data Availability. All study data are included in the article and/or *SI Appendix*.

ACKNOWLEDGMENTS. C.-W.Q. acknowledges financial support by the Ministry of Education, Republic of Singapore (Grant R-263-000-E19-114 | A-0005143-00-00). S.F. acknowledges the support by US Department of Energy (Grant DE-FG02-07ER46426). S.Z. acknowledges support by European Research Council Consolidator Grant (TOPOLOGICAL), the Royal Society, and the Wolfson

Foundation. D.N.C. acknowledges support by the Air Force Office of Scientific Research Multidisciplinary Research Program of the University Research Initiative (Grant FA9550-20-1-0322), Simon Foundation (Grant 733682), NSF (Grant DMR-1420620), and the United States-Israel Binational Science Foundation (Grant 2016381). W.L. acknowledges the support of National Natural Science Foundation of China (Grants 62134009 and 62121005), and the Innovation Grant of Changchun Institute of Optics, Fine Mechanics and Physics. X.Z. acknowledges the financial support of Chongqing Natural Science Foundation (Grant cstc2021jcyj-msxmX0627) and the Science and Technology Research Program of Chongqing Municipal Education Commission (Grant KJQN202000829). Y.L. acknowledges the financial support of National Natural Science Foundation of China (Grant 92163123).

Author affiliations: [a]Department of Electrical and Computer Engineering, National University of Singapore, Kent Ridge 117583, Republic of Singapore; [b]GPL Photonics Laboratory, State Key Laboratory of Applied Optics, Changchun Institute of Optics, Fine Mechanics and Physics, Chinese Academy of Sciences, Changchun 130033, China; [c]School of Computer Science and Information Engineering, Chongqing Technology and Business University, Chongqing 400067, China; [d]Interdisciplinary Center for Quantum Information, State Key Laboratory of Modern Optical Instrumentation, ZJU-Hangzhou Global Scientific and Technological Innovation Center, Zhejiang University, Hangzhou 310027, China; [e]International Joint Innovation Center, Key Laboratory of Advanced Micro/Nano Electronic Devices & Smart Systems of Zhejiang, The Electromagnetics Academy at Zhejiang University, Zhejiang University, Haining 314400, China; [f]Department of Electrical Engineering, Stanford University, Stanford, CA 94305; [g]Ginzton Laboratory, Stanford University, Stanford, CA 94305; [h]Department of Physics, University of Hong Kong, Hong Kong, China; [i]Department of Electrical & Electronic Engineering, University of Hong Kong, Hong Kong, China; and [j]Center for Research and Education in Optics and Lasers (CREOL), The College of Optics and Photonics, University of Central Florida, Orlando, FL 32816

1. J. Wang, S. C. Zhang, Topological states of condensed matter. *Nat. Mater.* **16**, 1062–1067 (2017).
2. L. Lu, J. D. Joannopoulos, M. Soljačić, Topological photonics. *Nat. Photonics* **8**, 821 (2014).
3. L. Lu *et al.*, TOPOLOGICAL MATTER. Experimental observation of Weyl points. *Science* **349**, 622–624 (2015).
4. T. Ozawa *et al.*, Topological photonics. *Rev. Mod. Phys.* **91**, 15006 (2019).
5. Z. Chen, M. Segev, Highlighting photonics: Looking into the next decade. e*Light* **1**, 2 (2021).
6. M. Xiao, W. Chen, W. He, C. T. Chan, Synthetic gauge flux and Weyl points in acoustic systems. *Nat. Phys.* **11**, 920–924 (2015).
7. G. Ma, M. Xiao, C. T. Chan, Topological phases in acoustic and mechanical systems. *Nat. Rev. Phys.* **1**, 281–294 (2019).
8. G. E. Volovik, *The Universe in a Helium Droplet* (Clarendon, Oxford, 2003).
9. W. Gao *et al.*, Experimental observation of photonic nodal line degeneracies in metacrystals. *Nat. Commun.* **9**, 950 (2018).
10. A. C. Potter, I. Kimchi, A. Vishwanath, Quantum oscillations from surface Fermi arcs in Weyl and Dirac semimetals. *Nat. Commun.* **5**, 5161 (2014).
11. W. Gao *et al.*, Photonic Weyl degeneracies in magnetized plasma. *Nat. Commun.* **7**, 12435 (2016).
12. L. Feng, Z. J. Wong, R. M. Ma, Y. Wang, X. Zhang, Single-mode laser by parity-time symmetry breaking. *Science* **346**, 972–975 (2014).
13. D. Leykam, K. Y. Bliokh, C. Huang, Y. D. Chong, F. Nori, Edge modes, degeneracies, and topological numbers in non-Hermitian systems. *Phys. Rev. Lett.* **118**, 040401 (2017).
14. B. Peng *et al.*, Parity-time-symmetric whispering-gallery microcavities. *Nat. Phys.* **10**, 394–398 (2014).
15. P. Miao *et al.*, Orbital angular momentum microlaser. *Science* **353**, 464–467 (2016).
16. B. Peng *et al.*, Chiral modes and directional lasing at exceptional points. *Proc. Natl. Acad. Sci. U.S.A.* **113**, 6845–6850 (2016).
17. H. Zhao *et al.*, Non-Hermitian topological light steering. *Science* **365**, 1163–1166 (2019).
18. B. Peng *et al.*, Loss-induced suppression and revival of lasing. *Science* **346**, 328–332 (2014).
19. H. Zhou *et al.*, Observation of bulk Fermi arc and polarization half charge from paired exceptional points. *Science* **359**, 1009–1012 (2018).
20. A. Cerjan *et al.*, Experimental realization of a Weyl exceptional ring. *Nat. Photonics* **13**, 623–628 (2019).
21. W. Wang, W. Gao, L. Cao, Y. Xiang, S. Zhang, Photonic topological fermi nodal disk in non-Hermitian magnetic plasma. *Light Sci. Appl.* **9**, 40 (2020).
22. L. Feng, R. El-Ganainy, L. Ge, Non-Hermitian photonics based on parity-time symmetry. *Nat. Photonics* **11**, 752 (2017).
23. B. Midya, H. Zhao, L. Feng, Non-Hermitian photonics promises exceptional topology of light. *Nat. Commun.* **9**, 2674 (2018).
24. Y. Xu, S. T. Wang, L. M. Duan, Weyl exceptional rings in a three-dimensional dissipative cold atomic gas. *Phys. Rev. Lett.* **118**, 045701 (2017).
25. A. Cerjan, M. Xiao, L. Yuan, S. Fan, Effects of non-Hermitian perturbations on Weyl Hamiltonians with arbitrary topological charges. *Phys. Rev. B* **97**, 075128 (2018).
26. Y. Li *et al.*, Anti-parity-time symmetry in diffusive systems. *Science* **364**, 170–173 (2019).
27. G. Xu, Y. Li, W. Li, S. Fan, C.-W. Qiu, Configurable phase transitions in topological thermal material. *Phys. Rev. Lett.* **127**, 105901 (2021).
28. T. Ozawa, H. M. Price, N. Goldman, O. Zilberberg, I. Carusotto, Synthetic dimensions in integrated photonics: From optical isolation to four-dimensional quantum Hall physics. *Phys. Rev. A (Coll. Park)* **93**, 043827 (2016).
29. A. Dutt *et al.*, A single photonic cavity with two independent physical synthetic dimensions. *Science* **367**, 59–64 (2020).
30. K. Wang *et al.*, Generating arbitrary topological windings of a non-Hermitian band. *Science* **371**, 1240–1245 (2021).
31. C. Z. Fan, Y. Gao, J. P. Huang, Shaped graded materials with an apparent negative thermal conductivity. *Appl. Phys. Lett.* **92**, 251907 (2008).
32. G. Xu *et al.*, Tunable analog thermal material. *Nat. Commun.* **11**, 6028 (2020).
33. S. Yang, J. Wang, G. L. Dai, F. B. Yang, J. P. Huang, Controlling macroscopic heat transfer with thermal metamaterials: Theory, experiment and application. *Phys. Rep.* **908**, 1–65 (2021).
34. M. Camacho, B. Edwards, N. Engheta, Achieving asymmetry and trapping in diffusion with spatiotemporal metamaterials. *Nat. Commun.* **11**, 3733 (2020).